ACS APPLIED MATERIALS & INTERFACES

Research Article

www.acsami.org

Facile Synthesis of Gold Nanospheres Modified by Positively Charged Mesoporous Silica, Loaded with Near-Infrared Fluorescent Dye, for in Vivo X-ray Computed Tomography and Fluorescence Dual Mode Imaging

Ji-Tao Song,[†] Xiao-Quan Yang,[†] Xiao-Shuai Zhang, Dong-Mei Yan, Zhao-Yang Wang, and Yuan-Di Zhao*

Britton Chance Center for Biomedical Photonics at Wuhan National Laboratory for Optoelectronics—Hubei Bioinformatics and Molecular Imaging Key Laboratory, Department of Biomedical Engineering, College of Life Science and Technology, Huazhong University of Science and Technology, Wuhan 430074, P. R. China

Supporting Information

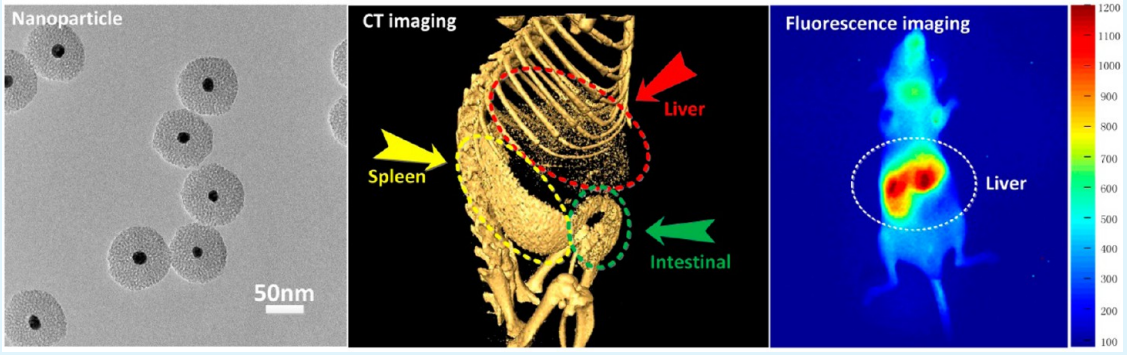

ABSTRACT: We developed a simple and efficient method to synthesize a novel probe for both computed tomography (CT) and fluorescence imaging. Gold nanospheres were coated with positively charged mesoporous silica (Au@mSiO$_2$-TTA) using a one-pot method to cohydrolyze quaternary ammonium silane and tetraethyl orthosilicate. Subsequently, IR-783, a negatively charged and water-soluble near-infrared fluorescent dye, was electrostatically adsorbed into the silica shell. Transmission electron microscopy imaging, X-ray powder diffraction, and energy dispersive X-ray spectroscopy indicated that Au@mSiO$_2$-TTA had a clear core−shell structure, was monodisperse, had a large surface area (530 m^2/g), and had a uniform pore size (2.2 nm). The mesoporous structure could effectively load fluorescent dye. After loading, the zeta potential of the nanoparticle dropped from 48 mV to 30 mV, and after additional modification with polyvinylpyrrolidone, it further reduced to 6 mV. Probe fluorescence was stable over time, and the probe was an effective CT contrast agent and as a near-infrared fluorescent probe. The half-life of the probe in the blood was 1.5 h, and the probe was mainly distributed in the spleen and liver 4 h after injection. Tissue sections showed that major organs were normal and without visible morphological changes, 6 days post injection, indicating the biocompatibility of the probe.

KEYWORDS: *CT imaging, NIR fluorescence imaging, Au nanoparticle, mesoporous silica, dual mode imaging*

INTRODUCTION

Multimode colocalized imaging can overcome the shortcomings of individual imaging techniques and realize the complementary advantages of multiple techniques; it can provide physicians and researchers with the information needed to make accurate and professional judgments regarding the location of lesions and optimal treatment plans.[1−6] At present, commonly used imaging methods in hospitals include X-ray projection imaging, X-ray computed tomography (CT) imaging, magnetic resonance imaging (MRI), ultrasonic imaging, and positron emission tomography (PET). Among the various imaging modalities, CT produces high spatial resolution and a computer-visualized 3D structure of deep tissue. With increasing detector sensitivity and increasing data processing speeds, the temporal and spatial resolution of CT continue to improve.[7,8] Nevertheless, conventional CT imaging is usually used to image high-density tissue, bone, stones, and other hard foreign objects, not for soft tissues with weak X-ray absorption such as tumors. CT imaging cannot be used to differentiate between the lesions and surrounding normal tissue because the two tissue types do not differ in X-ray absorption.[9] Therefore, contrast agents were used to enhance the difference between the irradiated tissues. Iodinated contrast agents are widely used in clinical applications because iodine has a high

Received: May 20, 2015
Accepted: July 20, 2015
Published: July 20, 2015

DOI: 10.1021/acsami.5b04359
ACS Appl. Mater. Interfaces 2015, 7, 17287−17297

atomic number and a high X-ray attenuation coefficient. However, iodinated agents are not used because they produce good contrast but because they are of low cost and low toxicity. In practice, iodinated agents must be used in large doses to achieve an obviously enhanced effect because these agents are quickly cleared by the kidneys and have a short circulation time.[10]

Nanoparticles are rapidly gaining importance for their application in nanobiotechnology owing to their large surface area and diverse constituent materials.[11−15] In recent years, nanoparticles containing Au, Bi, Ta, Lu, and Yb, all elements with high X-ray attenuation coefficients, have been used in CT imaging research.[16−21] Among them, gold nanoparticles (Au NPs) are low toxicity and easily modified.[22−24] However, considering that the sensitivity of CT is not high enough for imaging at the molecular and cellular levels, if a more highly sensitive imaging technique could integrate together with CT nanoparticle as a probe, the composite probe would be versatile in the level of structure that could be visualized.

Fluorescence imaging is a real-time, noninvasive, and sensitive imaging technique; it can provide cellular and even molecular level information and can be applied to biomedical detection. However, there are some obstacles to using fluorescence imaging in vivo including a low signal-to-noise ratio due to tissue autofluorescence and poor light penetration in the visible light range. Near-infrared (NIR) fluorescence materials overcome some of the obstacles encountered in fluorescence imaging in vivo; blood and tissues show minimal autofluorescence in the wavelength range of 700−1000 nm, minimizing intrinsic background interference. The 700−1000 nm range is a good window for imaging as it is possible to obtain a high signal-to-noise ratio.[25−27] However, fluorescence imaging suffers from low spatial resolution and limited penetration depth, even at NIR wavelengths. Therefore, it would be ideal to combine CT and fluorescence imaging to develop a complementary imaging method with high spatial resolution and high sensitivity.

To fabricate this kind of multifunctional composite probe, the most important issue is choosing the NIR fluorescent material. An ideal NIR fluorescent probe needs to meet the following basic requirements: both the excitation and fluorescence emission wavelengths should be in the NIR range for good tissue penetration and low attenuation; the Stokes shift should be large so that absorption and emission processes do not interfere with each other; the molar absorption coefficient and quantum yield should be high for strong fluorescence intensity; the chemical and photophysical properties should support a long luminescence time in solvent; the probe should be biocompatible and soluble in water to avoid dye aggregation in an aqueous environment; and the chemical stability should be sufficient under physiological conditions in vivo.[26] These requirements greatly narrow the choice of suitable materials. Current NIR probes fall into two categories: inorganic nanoparticles and organic molecules. Inorganic NIR contrast agents mainly consist of quantum dots (QDs) and other nanoparticles. It has been reported that some rare earth doped up-conversion materials (anti-Stokes) can meet the above requirements.[28−33] However, the up-conversion material usually requires a high energy laser for excitation and rare earth dopants are not naturally occurring in the body, both factors contributing to incompatibility with in vivo biological imaging. Compared with inorganic probes, organic NIR fluorescent dyes are very attractive candidates for imaging because the newly developed NIR dyes have improved photophysical properties, biocompatibility, high fluorescence quantum yields, and do not contain extra heavy metal elements, so they are amenable to large-scale chemical synthesis. Organic NIR fluorescent dyes can be compounded together with nanoparticles to make a multifunctional imaging probe. At present, the most common NIR dyes are cyanine dyes such as trimethine cyanines (Cy3), pentamethine cyanines (Cy5), heptamethine cyanines (Cy7), and their derivatives. The Food and Drug Administration has approved indocyanine green (ICG) for use as an indicator of blood flow and liver function for 60 years. However, poor photostability, low quantum yield, high plasma protein binding rate, undesired aggregation, and aqueous instability of free ICG has limited its application as a fluorescence contrast agent for in vivo imaging.[25,26]

Combining an NIR dye and Au nanoparticle is the second hurdle in constructing a multifunctional composite nanoprobe. Au nanoparticles can quench fluorescence within a certain distance, so the distance between the NIR dye and Au nanoparticle must be carefully controlled to avoid fluorescence quenching.[34,35] Because of its unique mesoporous structure, mesoporous silica ($mSiO_2$) is broadly applied in biotechnology. $mSiO_2$ has many pores and a large surface area; the pores can be used as chambers for loading NIR dyes, and the expansive surface area can be easily modified by functional molecules including the binding of NIR dyes.[36,37] Further, $mSiO_2$ is biocompatible and is optically transparent, meaning that light can easily penetrate $mSiO_2$ to excite internal NIR dyes in mesopores. In a previous study, ICG was reacted with aminopropyltrimethoxysilane (APTES), and the resulting molecule was used to modify the surface of a gold nanorod coated with $mSiO_2$, which was then used as a CT/fluorescence bifunctional probe.[38] However, the fluorescent dye binding rate was low using this particular modification method, and the approach did not make full use of the advantages of $mSiO_2$ for loading additional ICG into the mesopores; the fast hydrolysis speed of APTES is likely to cause the aggregation of nanoparticles, resulting in poor dispersion, which is not useful for in vivo application. Further, gold nanorods have strong absorption in the NIR spectral region, greatly reducing the intensity of NIR excitation and fluorescence emission. In aqueous solution or blood plasma, ICG undergoes physico-chemical transformations, such as aggregation and irreversible degradation, which reduce its fluorescence quantum efficiency.[26] Together, these results suggest that the combination of gold nanorods and NIR dye was not conducive to in vivo imaging. It is crucial to look for other suitable NIR fluorescent dyes that can be easily and substantially loaded into $mSiO_2$.

IR-783 is a new type of water-soluble cyanine dye with a rigid cyclohexenyl substitution introduced into the middle of a polymethine linker and a substituted central chlorine atom in the cyclohexene ring, which together, remarkably increased the photostability and fluorescence quantum yield. It was also found that IR-783 was biocompatible and did not accumulate in normal cells.[39,40] Therefore, it has some features of an ideal NIR fluorescent dye. If the pores of $mSiO_2$ could be modified with a cluster of positive charge, IR-783 could easily enter into the $mSiO_2$ channels by electrostatic adsorption, as its two sulfonic acid groups have a strong negative charge. The large surface area and pore volume of $mSiO_2$ could load a large number of IR-783 molecules, and once loaded into pores, the

DOI: 10.1021/acsami.5b04359
ACS Appl. Mater. Interfaces 2015, 7, 17287−17297

Scheme 1. Schematic Illustration of the Synthetic Procedure. Positively-Charged Mesoporous Silica Modified Gold Nanospheres Loaded with Near-Infrared Fluorescent Dye for in Vivo X-Ray CT and Fluorescence Dual Mode Imaging

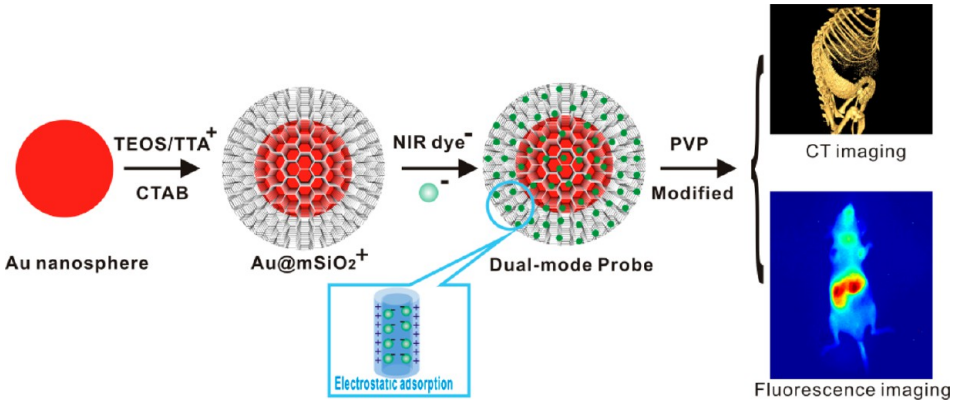

IR-783 molecules could effectively resist external environment changes.

In this paper, we used positively charged $mSiO_2$ to directly coat Au nanospheres by cohydrolysis of N-trimethoxysilylpropyl-N,N,N-trimethylammonium chloride (TTA) and tetraethoxysilane (TEOS). The hydrolysis rate of TTA is slower than that of APTES, which ensures that nanoparticles will not agglomerate during the process of coating the $mSiO_2$ shell.[41] We found that the positively charged $mSiO_2$ maintained mesoporous structure, IR-783 could be easily adsorbed into the mesoporous structure through electrostatic interaction, and the method of fabricating the composite nanoparticle Au@$mSiO_2$-TTA/IR-783 was simple and effective. The probe Au@$mSiO_2$-TTA/IR-783/PVP could be used for CT and fluorescence imaging, both in vitro and in vivo, after being modified with polyvinylpyrrolidone (PVP). Therefore, this multifunctional nanoprobe is expected to be effective for both vascular tumor imaging and biomedical research.

EXPERIMENTAL SECTION

Materials and Instruments. Chloroauric acid ($HAuCl_4 \cdot 4H_2O$), TEOS, hydrochloric acid (HCl), ammonia ($NH_3 \cdot H_2O$), polyvinylpyrrolidone K30 (PVP-K30), and cetyltrimethylammonium bromide were purchased from Sinopharm. TTA (50% in methanol) was purchased from China Beijing J&K Chemical Scientific Co. Ltd. The heptamethine cyanine dye IR-783 (2-[2-[2-chloro-3-[2-[1,3-dihydro-3,3-dimethyl-1-(4-sulfobutyl)-2H-indol-2-ylidene]-ethylidene]-1-cyclohexen-1-yl]-ethenyl]-3,3-dimethyl-1-(4-sulfobutyl)-3H-indolium) was purchased from Sigma-Aldrich. Male nude mice (body weight 20–22 g) were purchased from the animal experimental center of Hubei Provincial Epidemic Prevention Station. The instruments include Tecnai G2 20 U-Twin 200 kV high-resolution transmission electron microscope (FEI, USA); Nano-ZS90 Zatasizer (Malvern, UK); VERTEX 70 Fourier-transform infrared spectrometer (Bruker, Germany); Empyrean B.V. X-ray diffractometer (PANalytical, Holland); LS45/55 luminescence spectrophotometer (PerkinElmer, USA); novAA400 absorption spectrometer (Jena atomic, Germany); Self-build wide-field fluorescence imaging optical system[42] (light filter wavelength used for fluorescence imaging was set at 700 ± 8 nm in excitation with fwhm of 40 ± 8 nm, at 808 ± 8 nm in emission with fwhm of 40 ± 8 nm), and CT imaging system[43] (spatial resolution is 100 μm, tube voltage is 50 kV, tube current is 0.8 mA). All animal experimental operations were approved by Huazhong University of Science and Technology animal ethics committee.

Synthesis of Au@$mSiO_2$-TTA Nanoparticles. Au nanoparticles coated with TTA-doped $mSiO_2$ (Au@$mSiO_2$-TTA) were prepared as follows. $HAuCl_4$ solution (3.5 mL, w/v 1%) was added to 150 mL of ultrapure water and heated to boiling under stirring. Sodium citrate solution (6 mL, w/v 1%) was rapidly injected, and the resulting mixture was boiled for another 30 min. Then the Au colloid was slowly cooled down to room temperature. Without any further treatment, the resultant colloidal gold solution was directly added to 10 mL of CTAB solution (0.1 M), the mixture was stirred for another 15 min, ammonia was added to adjust the pH value to 10, and the solution was stirred for another 10 min. According to the requirements, Au@$mSiO_2$ with different thicknesses of $mSiO_2$ could be obtained by changing the amount of TEOS. After TEOS was added, the reaction continued to react for 10 h at room temperature. As an example, the synthesis of 75 nm Au@$mSiO_2$-TTA is described. TEOS (240 μL) was added and reacted for 3 h, and then 100 μL of TTA methanol solution, together with 100 μL of TEOS, was added and reacted for 10 h before finishing. The sediment was collected by centrifugation and dispersed in ethanol by sonication, and then hydrochloric acid was added until the pH was less than 1. After 30 min, the sample was centrifuged and dispersed again. The final product, Au@$mSiO_2$-TTA, was obtained after alternately washing with ethanol and water and was then stored in ethanol at the original Au colloid concentration.

Synthesis of the Au@$mSiO_2$-TTA/IR-783/PVP Probe. Eighty milliliters of Au@$mSiO_2$-TTA was mixed with IR-783 ethanol solution (after mixing, the final concentration of IR-783 was 50 nM) and kept for 2 h to obtain full absorption. After alternate washing with ethanol and centrifugation, Au@$mSiO_2$-TTA/IR-783 composite nanoparticles were obtained. Five milliliters of PVP-K30 aqueous solution (0.1 mg/mL) was added to the sediment and dispersed by sonication. After 30 min, the solution was centrifuged to remove the excess PVP, and an appropriate amount of water was added to make an Au@$mSiO_2$-TTA/IR-783/PVP probe solution.

Au@$mSiO_2$-TTA/IR-783/PVP for CT and Fluorescence Imaging in Vitro. The probe was prepared at different concentrations. The Au concentrations were 4.5, 9, 13.5, 18, 22.5, and 28 mg/mL, and the probe CT imaging was carried out using a self-built CT imaging system. The NIR fluorescent imaging was carried out using a self-built wide-field fluorescence imaging optical system, and Au concentrations were 0.025, 0.05, 0.1, 0.2, and 0.4 mg/mL. Phagocytosis and the fluorescence stability of the Au@$mSiO_2$-TTA/IR-783/PVP probe were observed both inside and outside of cells. RAW 264.7 cells (murine macrophage cell line) were cultured in Dulbecco's Modified Eagle's Medium supplemented with 10% (v/v) newborn calf serum and penicillin/streptomycin (100 U/mL and 100 μg/mL, respectively) in a humidified atmosphere of 5% CO_2 at 37 °C for 48 h. The culture medium was exchanged for medium containing the probe at concentration of 0.1 mg/mL for another 48 h. After that, the cells were washed with PBS and then fixed in 4% paraformaldehyde for 30 min. Some cells were scraped from the dish bottom, collected by centrifugation, and embedded in resin. Cell sections were observed under the electron microscope. Another cell sample was immersed in 4% paraformaldehyde for fluorescence imaging.

Au@$mSiO_2$-TTA/IR-783/PVP for CT and Fluorescence Imaging in Vivo. Nude mice were injected with probe at a dose of 200 μL,

DOI: 10.1021/acsami.5b04359
ACS Appl. Mater. Interfaces 2015, 7, 17287–17297

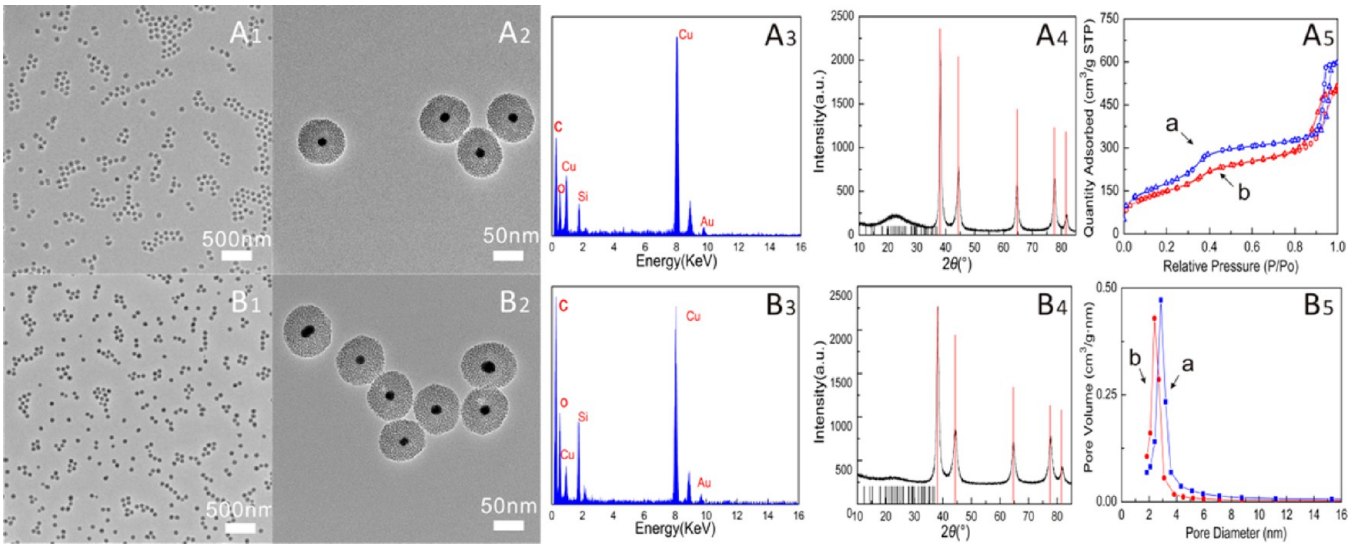

Figure 1. Characterizations of (A) Au@mSiO$_2$ and (B) Au@mSiO$_2$-TTA. (A_1, A_2, B_1, B_2) TEM under different magnifications; (A_3, B_3) EDX; (A_4, B_4) XRD, the red lines corresponding to the diffraction peaks of Au, the JCPDS standard is No. 02−1095, the black lines corresponding to the diffraction peaks of SiO_2, the JCPDS standard is No. 50−0057; (A_5) N_2 adsorption−desorption isothermal curves and (B_5) pore size distribution curves of (a) Au@mSiO$_2$ and (b) Au@mSiO$_2$-TTA.

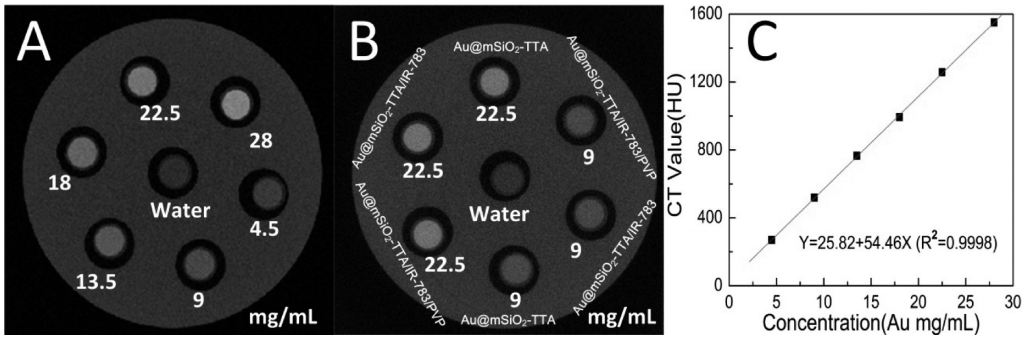

Figure 2. (A)CT imaging of different concentrations of the Au@mSiO$_2$-TTA/IR-783/PVP probe; (B) CT imaging of the same concentrations of Au@mSiO$_2$-TTA, Au@mSiO$_2$-TTA/IR-783, and Au@mSiO$_2$-TTA/IR-783/PVP, respectively; (C) the relationship between the concentrations and Hounsfield unit (HU) values; and the concentrations of probe are labeled as Au concentrations. The corresponding concentrations (mg/mL) of each sample are provided beside the respective images.

at a probe concentration of 50 mg/mL. CT imaging of nude mice was carried out using a self-built CT imaging system. The CT image was acquired prior to injection of Au@mSiO$_2$-TTA/IR-783/PVP as well as at appropriate time points after administration. To ensure the imaging position was stable, mice were anesthetized through intraperitoneal injection of chloral hydrate and urethane at a 1:1 ratio (10 wt %, respectively). NIR fluorescence imaging of nude mice was carried out using a self-built wide-field fluorescence imaging system. Male nude mice were randomly divided into two groups, and probe was injected into mice by tail vein injection. One group was dissected 1, 2, 4, 12, 24, and 48 h after injection (three mice were anatomized at each time point). The hearts, lungs, livers and spleens, kidneys, and intestines were collected and weighed after cardiac perfusion. These organs were ground and digested with aqua regia. After centrifugation and appropriate dilution, the concentrations of Au were measured by atomic absorption spectroscopy (AAS) and used to examine the probe distribution in mice organs. Blood specimens were collected from another group via the orbital venous plexus 5 min and 0.5, 1, 3, 6, 10, 16, and 24 h after injection (blood from three mice was collected at each time point). The blood was also digested with aqua regia. After appropriate depuration, the concentrations of Au were measured by AAS to investigate the metabolism of the probe in the blood. To characterize probe toxicity in vivo, the heart, liver, spleen, lung, kidney, and intestine were cut into thin slices and stained with hematoxylin−eosin (HE) to observe tissue morphology.

RESULTS AND DISCUSSION

The Au nanoparticle was synthesized by sodium citrate reduction, a well-characterized and widely used method. Sodium citrate was adsorbed onto the surface of the Au nanoparticle as a reducing agent and stabilizer. The nucleation time was short. The synthesized gold colloidal solution was directly added to an aqueous solution of CTAB, and then TTA and TEOS cohydrolyzed on the surface of the Au nanoparticle, forming a positively charged mSiO$_2$ shell under alkaline conditions (Scheme 1). This one-pot, two-step synthetic method greatly simplified the experimental procedure but was of high efficiency and high yield. Transmission electron microscopy (TEM) results showed that the Au@mSiO$_2$-TTA particle had a core−shell structure with a 20 nm diameter gold core (Figure 1B_1,B_2), and the mesopores were well-distributed on the mSiO$_2$ shell. There were no visible morphological changes compared with Au@mSiO$_2$ without TTA (Figure 1A_1,A_2). Au@mSiO$_2$-TTA was well dispersed, had a uniform particle size distribution, and exhibited no particle adhesion, factors that indicate the probe is suitable as an in vivo imaging agent. Energy dispersive X-ray spectroscopy (EDX) and X-ray diffraction (XRD) of the particle showed that there were no

DOI: 10.1021/acsami.5b04359
ACS Appl. Mater. Interfaces 2015, 7, 17287−17297

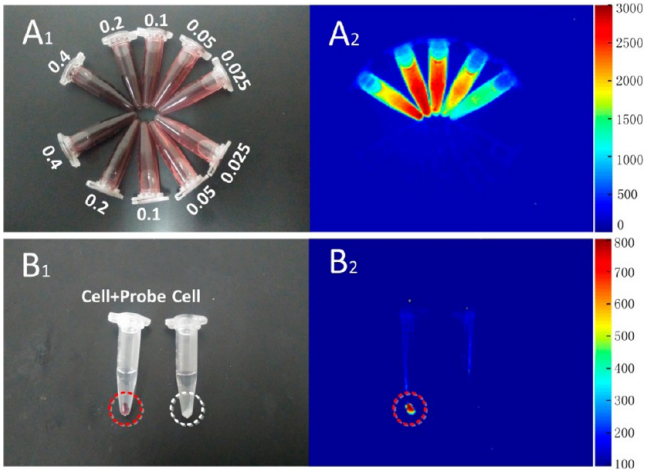

Figure 3. (A_1) Visible light image and (A_2) fluorescence image of different concentrations of Au@$mSiO_2$-TTA (lower half) and Au@$mSiO_2$-TTA/IR-783/PVP (upper half). The corresponding concentrations (mg/mL) of each sample are provided beside the respective images. (B_1) Visible light image and (B_2) fluorescence image of concentrated collected RAW 264.7 macrophages incubated with probe for 48 h. The excitation filter wavelength was set to 700 ± 8 nm, fwhm 40 ± 8 nm, and the emission filter wavelength was set to 808 ± 8 nm, fwhm 40 ± 8 nm.

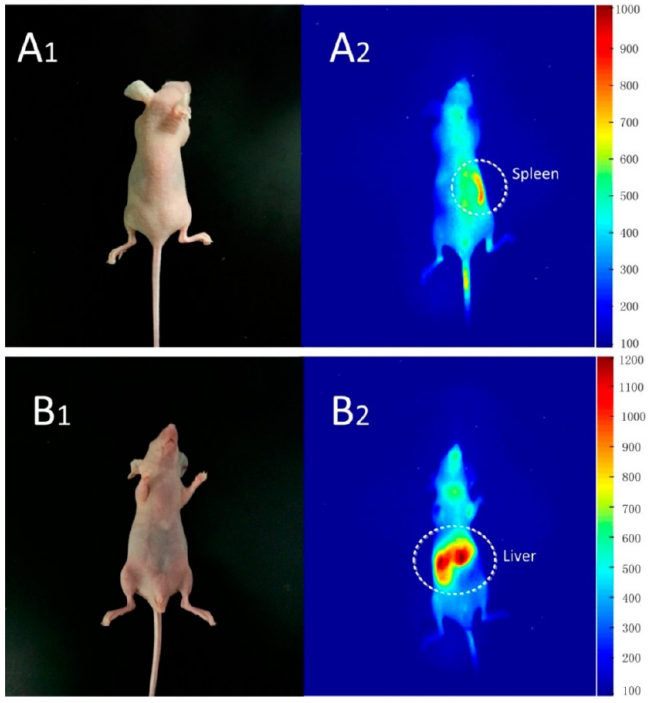

Figure 5. Images of nude mice 4 h after probe injection, from the (A) back side and (B) abdominal side using (1) bright field and (2) NIR fluorescence.

differences in basic composition or structure between the pure Au@$mSiO_2$ (Figure 1A_3,A_4) and the Au@$mSiO_2$-TTA composite particles (Figure 1B_3,B_4).

The surface area and pore volume of Au@$mSiO_2$-TTA determined the loading capacity of $mSiO_2$. A thick $mSiO_2$ shell has a larger surface area and higher loading capacity. A larger amount of NIR fluorescent dye IR-783 is likely to produce stronger fluorescence intensity and a higher signal-to-noise ratio. However, a thicker $mSiO_2$ shell might decrease the CT imaging effectiveness per unit mass, meaning that the Au@$mSiO_2$-TTA particle size should be moderate. Consequently, the $mSiO_2$ shell of the Au@$mSiO_2$-TTA particle should be sufficiently thick to ensure sufficient loading of IR-783 and to prevent IR-783 from quenching by the Au nuclear core (studies have shown that fluorescence quenching occurred when the fluorescent molecule was close to the Au nanoparticle[44]) but thin enough to improve CT X-ray absorption per unit mass of the probe. To balance these opposing size limitations, the size of the diameter of the Au@$mSiO_2$-TTA particle was made 75 nm, and the thickness of the $mSiO_2$ shell was about 27 nm. The N_2 adsorption−desorption isotherm curve indicated that the resulting Au@$mSiO_2$-TTA particle had a high Brunauer−Emmett−Teller (BET) surface area (530 m^2/g), large pore volume (0.8 cm^3/g), and uniform pore size (2.2 nm). A similarly sized Au@$mSiO_2$ particle possessed a slightly larger surface area (620 m^2/g), pore volume (0.9 cm^3/g), and pore size (2.5 nm). Although the pore volume and surface area slightly decreased after doping with TTA, it still maintained a relatively high surface area and pore volume and should effectively load dyes (Figure 1A_5,B_5).

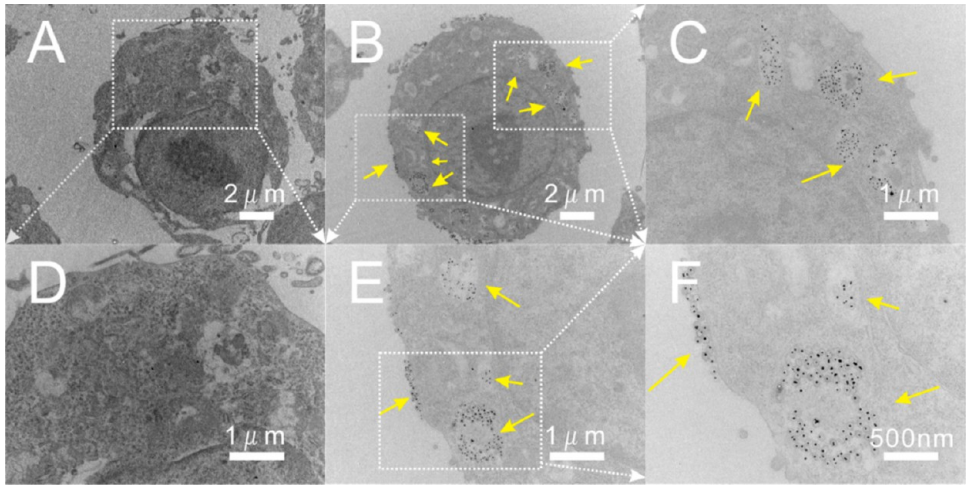

Figure 4. TEM images of ultrathin slices of (A) RAW264.7 cells alone and (B) incubated with Au@$mSiO_2$-TTA/IR-783/PVP for 48 h. Panel D is an enlarged image from a region of panel A; Panels C, E, and F are enlarged images from regions of panel B.

DOI: 10.1021/acsami.5b04359
ACS Appl. Mater. Interfaces 2015, 7, 17287−17297

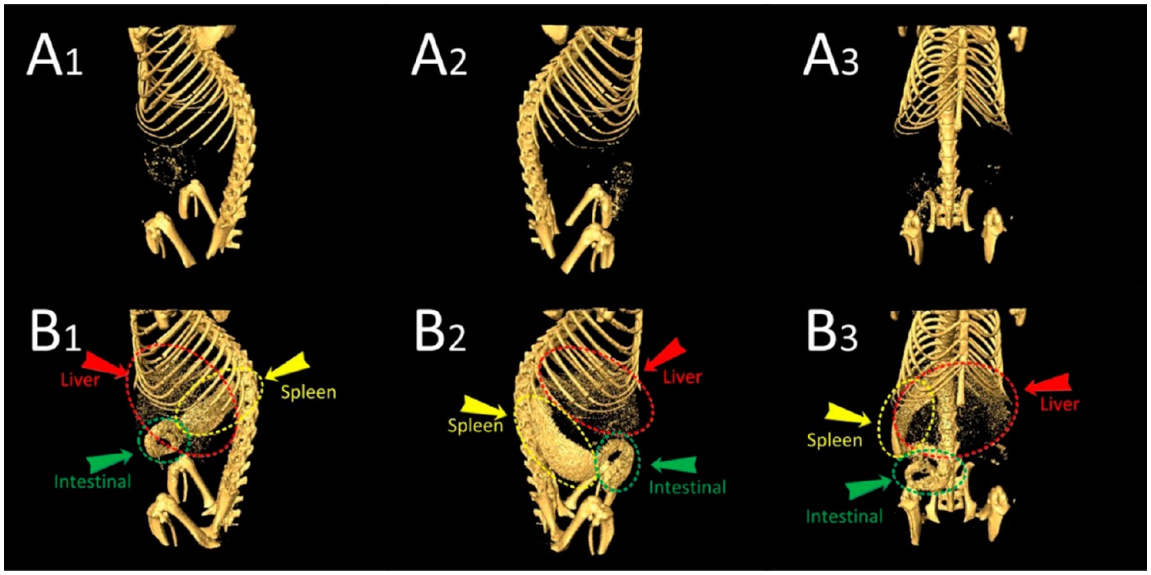

Figure 6. CT images of nude mice (A) before and (B) 4 h after injection from different views (1−3).

Au@mSiO$_2$ had a strong negative potential (−40 mV), and Au@mSiO$_2$-TTA possessed a very strong positive potential (+48 mV) after doping with TTA (Figure S1A, Supporting Information). Once the negatively charged NIR fluorescent dye IR-783 was mixed with the positively charged Au@mSiO$_2$-TTA, IR-783 adsorbed onto the Au@mSiO$_2$-TTA through electrostatic adsorption between sulfonic groups (negatively charged) and quaternary ammonium silane (positively charged). Knowing whether IR-783 attaches firmly is very important for in vivo use. If IR-783 can easily dissociate from mSiO$_2$, the fluorescence of the composite probe would gradually become weak, which is not beneficial to multifunctional imaging. However, we found that the probe fluorescence intensity and wavelength were stable over time after the excess dye was washed from the particles twice. The fluorescence intensity in the washes declined rapidly after several rounds of washing. It became very weak after the third round, indicating that IR-783 had firmly adsorbed onto the Au@mSiO$_2$-TTA particle (Figure S2A, Supporting Information). We also found that the fluorescence wavelength of the washing liquid (803 nm, Figure S2Ba, Supporting Information) was slightly shorter than the wavelength of the fluorescent probe (812 nm, Figure S2Aa, Supporting Information), which might be due to the Au@mSiO$_2$-TTA particle strongly attracting a large number of IR-783, which aggregated and caused a red shift.[45,46] Even if the probe was washed three times, the IR-783 was still difficult to wash off due to its strong binding ability, and the wavelength of the probe still showed a red shift (810 nm, Figure S2Ac, Supporting Information). This phenomenon indicates that the mutual adsorption capacity is very strong and that Au@mSiO$_2$-TTA was able to capture a large number of IR-783 molecules from the solution. The dye must have a very slow off-rate once absorbed onto the Au@mSiO$_2$-TTA particle. Both electrostatic interactions and the complementary shape of the pore's binding pocket may contribute to stable loading. When the dyes entered the mesoporous structure, they docked similar to ships in the harbor. The dyes were tightly bound in the small chamber spaces of the mesoporous silica where the surrounding environment was more stable and the dyes were less vulnerable to external disturbances. The dye was shielded from washing and substitution by homogeneously charged molecules. With washing, weakly bound fluorescent dye directly exposed to the external solvent would dissociate, while the tightly bound internal dye would not, explaining why the fluorescence intensity of the washes decreased until the third wash, where it was minimal. The red shift phenomenon was also observed for IR-783 alone in solution under different concentrations (Figure S3, Supporting Information). Along with the red shift, the fluorescence intensity was reduced, indicating that an appropriate ratio of Au@mSiO$_2$-TTA to IR-783 is important for fabricating a complex probe with high luminous intensity. When the concentration of IR-783 was 50 nM in Au@mSiO$_2$-TTA solution, the potential of purified Au@mSiO$_2$-TTA/IR-783 dropped down to about +30 mV (Figure S1A, Supporting Information), meaning that the probe was not yet saturated with IR-783, but since spectral changes such as the red shift and drop in signal intensity also occurred at 50 nM, more adsorption of IR-783 would not necessarily increase fluorescence intensity. Therefore, 50 nM was chosen as the final concentration of IR-783.

The dye loading capability of the mesoporous silica shell could be measured by the amount of IR-783 per unit area. Using the synthesis of the Au@mSiO$_2$-TTA/IR-783/PVP probe as an example, the mass of Au@mSiO$_2$-TTA was composed of two parts, the mass of gold particles and the mass of mesoporous silica. The gold nanoparticles came from the reduction of chloroauric acid, and the mesoporous silica was derived from the hydrolysis and polymerization of TEOS and TTA. The mass of Au@mSiO$_2$-TTA was calculated to be about 0.0648 g. The specific surface area of the Au@mSiO$_2$-TTA particle was 530 m^2/g, and the surface area of the product under experimental conditions was 33.48 m^2. The amount of IR-783 adsorbed into the mesoporous silica shell was equal to the initial amount added minus the remaining amount in the discarded washes. Within the linear range of the instrument, the fluorescence intensity of the solution is proportional to the concentration of the substance in the solution, so the ratio of the residual dye can be calculated by the fluorescence intensity. Using the fluorescence intensity of the original solution and the washes (Figure S2B, Supporting Information), we calculated that the amount of fluorescent dye adsorbed into the mesoporous silica per unit area was about 8.4×10^{-14} mol/cm^2.

DOI: 10.1021/acsami.5b04359
ACS Appl. Mater. Interfaces 2015, 7, 17287−17297

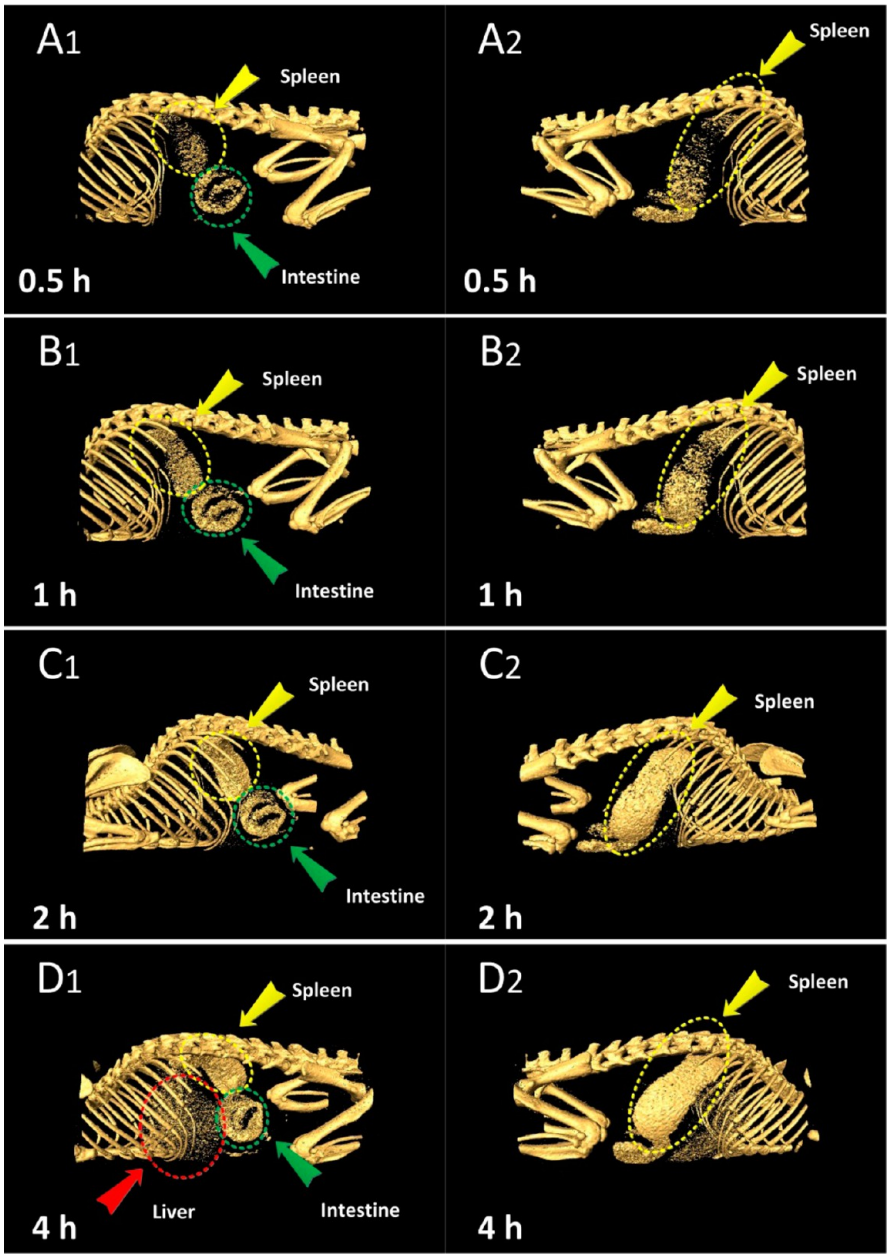

Figure 7. CT images of nude mice injected with the probe (A, 0.5 h; B, 1 h; C, 2 h; and D, 4 h after injection) from different views (1 and 2).

Since macrophages will strongly phagocytize the positively charged nanoparticles, it is necessary to further modify Au@ $mSiO_2$-TTA/IR-783 to avoid this complex probe form being quickly engulfed and cleared.[47,48] PVP-K30 is water-soluble, biocompatible, and adsorbs to the surface of silica. PVP-K30 can shield against blood proteins adsorbing onto the surface of the probe and can reduce the immunogenicity of the probe. Furthermore, PVP-K30 is a nonionic surface active agent, and it can effectively reduce the surface potential of probe, improving probe dispersion and viscosity.[49,50] Therefore, PVP-K30 was used to further modify the probe. The results indicate that the probe potential declined to +6 mV (Figure S1A, Supporting Information) after modification; the hydrated diameter changed from 158 to 160 nm but not significantly (Figure S2B, Supporting Information). Since this is the hydrated diameter, it is larger than the size obtained from the transmission electron microscope.

Fourier transform infrared (FT-IR) was used to characterize the composite particles (Figure S4, Supporting Information). In addition to the absorption of SiO_2 (1091−1095 cm^{-1}), methylene and methyl C−H asymmetric stretching vibration appeared at 2925 and 2982 cm^{-1}, respectively, after TTA doping; C−C skeleton bound vibration appeared at 1140−1250 cm^{-1} after IR-783 adsorption; CH_2 bending and deformation appeared at 1466 and 1426 cm^{-1}, respectively; and C═O stretching vibration was found at 1664 cm^{-1} after PVP modification.[51] The four curves indicate that TTA, IR-783, and PVP-K30 were assembled onto the nanoparticle step by step during the reaction.

Probe for CT and Fluorescence Imaging in Vitro. Au possesses a high X-ray attenuation coefficient, and CT imaging of different concentrations of Au@$mSiO_2$-TTA/IR-783/PVP (Figure 2A) produced different CT values; CT values increased linearly with Au concentrations (Figure 2C). Differences

DOI: 10.1021/acsami.5b04359
ACS Appl. Mater. Interfaces 2015, 7, 17287−17297

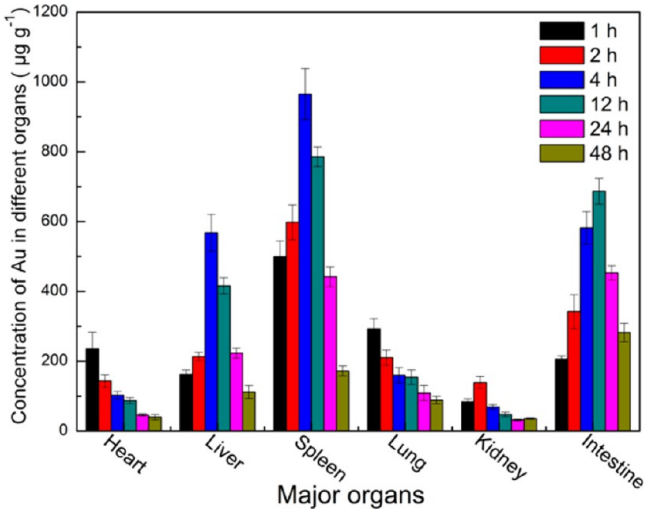

Figure 8. Distribution of probe changed with time in different organs of mice.

between CT images of Au@mSiO$_2$-TTA and Au@mSiO$_2$-TTA/IR-783/PVP were not evident (Figure 2B). NIR fluorescent imaging of different probe concentrations was also conducted. The fluorescence intensity became stronger with increased probe concentration. However, since Au@mSiO$_2$-TTA had no NIR fluorescent dye, in contrast to Au@mSiO$_2$-TTA/IR-783/PVP, it did not produce a fluorescent signal (Figure 3A$_2$). Strong fluorescence intensity could be obtained when the probe concentration over 0.1 mg/mL. Very high concentrations would slightly weaken the fluorescence intensity. The composite probe and cells were coincubated for 48 h. It was found that once the probe entered the cells, the color of the enriched cells changed from white to a red wine color, which was the color of the Au nanoparticles (Figure 3B$_1$). The cells containing the probe produced strong NIR fluorescence, while the control cells without probe added produced no fluorescence. Strong fluorescence intensity was stable over time within the cells, and there were no adverse quenching effects due to phagocytosis (Figure 3B$_2$). Ultrathin sections of cells were observed under TEM. Compared with the control cells (Figure 4A), there were many black particles in the enriched cells, and the probe was internalized into the cytoplasm (Figure 4B).

Probe for CT and Fluorescence Imaging in Vivo. A nanoprobe for in vivo application needs to be sufficiently stable

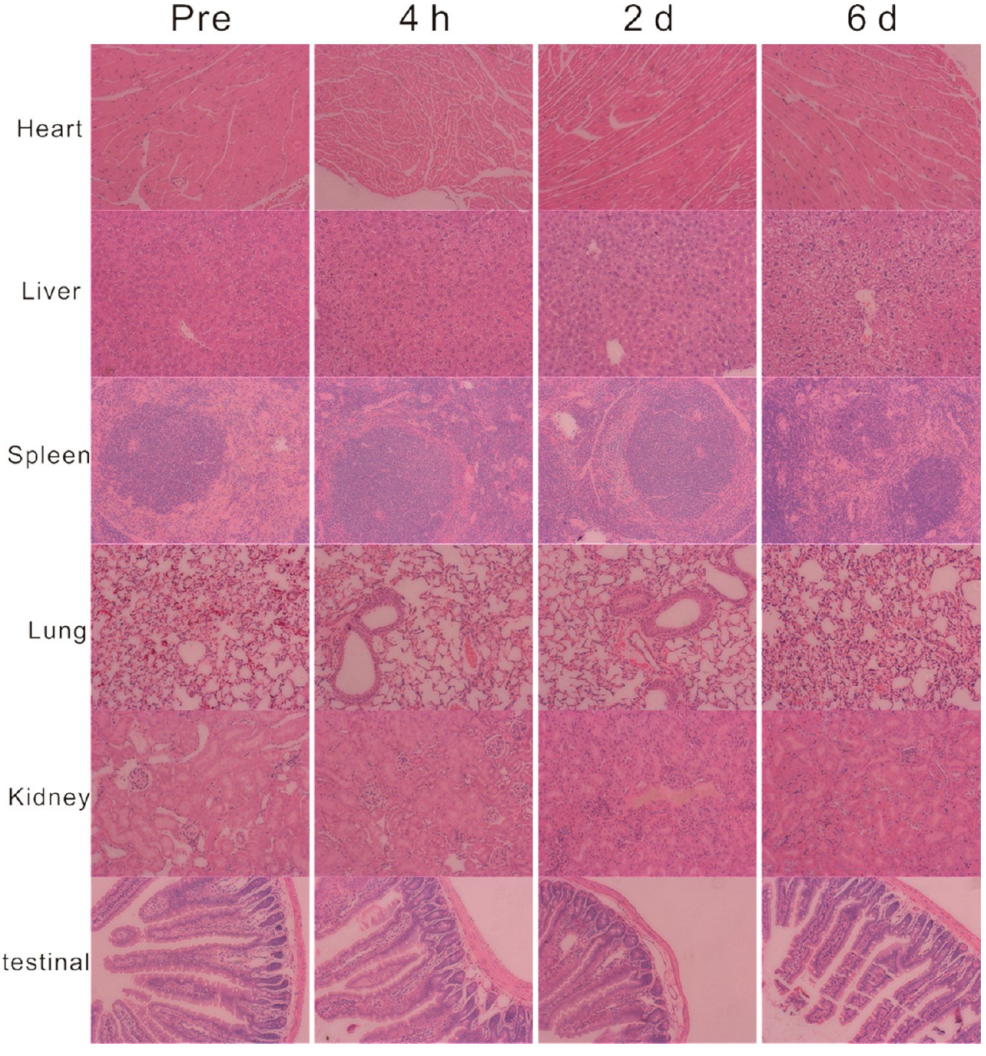

Figure 9. Tissue sections (heart, liver, spleen, lung, kidney, and intestine) stained with HE. Control mice without probe injection (Pre) and mice 4 h, 2 d, and 6 d after probe injection.

DOI: 10.1021/acsami.5b04359
ACS Appl. Mater. Interfaces 2015, 7, 17287−17297

in serum and should have a long blood circulation time so that the target position can be reached. Fluorescent probe, culture medium containing serum, and cells were coincubated for 48 h. The fluorescence intensity of the culture medium remained unchanged, indicating that the probe was stable (Figure S5, Supporting Information). The outstanding performance of the multifunctional probe in vitro suggested that the probe should also be effective in vivo. The probe was injected into male nude mice through the tail vein, and then fluorescence imaging (Figure 5) and X-ray CT imaging (Figure 6) were completed after 4 h.

As can be seen, the probe was mainly distributed in the spleen and liver, which could be visualized in high resolution using both fluorescence and CT imaging. We note that the liver fluorescence was superior to spleen fluorescence, while the CT of the spleen was superior to the CT of the liver. We speculate that the spleen might be richer in probe than the liver, which partially weakened the fluorescence intensity. It was found that part of the intestine produced an enhanced CT effect, and this phenomenon was also observed in previous studies using other nanoparticles.[11,12,33,52]

CT imaging of nude mice was also performed at different time points after probe injection (0.5, 1, 2, and 4 h). The probes first appeared in the spleen and intestinal tract and then appeared in the liver (Figure 7), indicating that the probe selectively accumulates in different organs. The concentration of probe in the blood was also measured. The probe concentration in the blood decreased from the initial 2 mg/mL to 150 μg/mL after 6 h (Figure S6, Supporting Information), and the half-life of the probe was 1.5 h. Together with the CT results, these results suggest that mononuclear phagocytes in the liver and spleen probably engulf probes, which explains why most of the probe in the blood accumulated in these organs. The enrichment of probe significantly increased the HU value for these organs and enhanced CT performance. The concentration of probe in the blood showed a downward trend, and the concentration was very low after 24 h.

We also conducted elemental analysis of the different organs at different time points after probe injection (Figure 8), and we found that the probe was widely distributed among the main organs including the liver, spleen, lung, and intestinal tract. The concentration of probe in the heart gradually declined over time, probably because the concentration of probe in the heart is just a reflection of the concentration of probe in the blood. The test concentration of probe in the liver, spleen, and intestine gradually increased over 1−4 h (Figure 7). After 24 h, the probe concentration remained high in the liver, spleen, and intestine, indicating that the probe is metabolized very slowly in these organs.

Although organ element analysis showed that the lungs also possessed a high probe concentration, the CT image did not capture the shape of the lung. Because of the negative pressure in the pleural cavity, the internal lung is swollen and full of gas in this physiological state, resulting in a large volume and low density, appearing blurry in the fluorescence image. After 48 h, there was a significant decrease in probe concentration in various organs. The concentration of Au was higher in the intestinal tract than in the liver and spleen after 48 h, indicating that the probe had been gradually excreted out of the body. It is important to know whether the probe had a negative effect on the health of the organs. Hence, mice injected with probe were eviscerated, and the organs were stained with HE to investigate morphology. The main tissues and organs were normal, without visible morphological changes (Figure 9) after 6 days, meaning the probe was biocompatible.

CONCLUSION

In this paper, a composite nanoparticle (Au@mSiO$_2$-TTA) coated with positively charged mesoporous silica was prepared using a one-pot method. NIR fluorescent dye was absorbed onto the surface by electrostatic interactions, and then CT and fluorescence dual mode imaging was carried out to characterize the probe. The method was simple and efficient. Experimental results in vitro and in vivo indicate that the probe was effective as a CT contrast agent and as a near-infrared fluorescent probe. With further improvement and optimization, this multifunctional nanoparticle could be expected to play an important role in CT/fluorescence dual mode imaging.

ASSOCIATED CONTENT

Supporting Information

Zeta potential and size distribution of Au@mSiO$_2$, Au@mSiO$_2$-TTA, Au@mSiO$_2$-TTA/IR-783, and Au@mSiO$_2$-TTA/IR-783/PVP; the fluorescent maps of Au@mSiO$_2$-TTA/IR-783 composite probe resuspension and its washing liquid supernatant after several rounds of washing and centrifugation; fluorescence emission spectra and absorption spectrum of different concentration of IR-783; the FT-IR maps of Au@mSiO$_2$, Au@mSiO$_2$-TTA, Au@mSiO$_2$-TTA/IR-783, and Au@mSiO$_2$-TTA/IR-783/PVP; the fluorescent curves of culture media before and after Au@mSiO$_2$-TTA/IR-783/PVP, serum and cells being coincubated for 48 h; and curve of probe concentration changed with time in blood. The Supporting Information is available free of charge on the ACS Publications website at DOI: 10.1021/acsami.5b04359.

AUTHOR INFORMATION

Corresponding Author

*E-mail: zydi@mail.hust.edu.cn. Phone: +86 27-8779-2202. Fax: +86 27-8779-2202.

Author Contributions

†These authors contributed equally.

Notes

The authors declare no competing financial interest.

ACKNOWLEDGMENTS

This work was supported by the National Natural Science Foundation of China (Grant No. 81271616, 81471697), the Foundation for Innovative Research Groups of the NNSFC (Grant No. 61121004), the Natural Science Foundation of Hubei Province (2014CFB1010), the Key Technology R&D Program of Hubei Province (2014BBB003) and Yellow Crane Talent (Science and Technology) Program of Wuhan City. We also thank the Analytical and Testing Center (HUST) for the help of measurement.

REFERENCES

(1) Fan, W.; Shen, B.; Bu, W.; Chen, F.; Zhao, K.; Zhang, S.; Zhou, L.; Peng, W.; Xiao, Q.; Xing, H.; Liu, J.; Ni, D.; He, Q.; Shi, J. Rattle-Structured Multifunctional Nanotheranostics for Synergetic Chemo-/Radiotherapy and Simultaneous Magnetic/Luminescent Dual-Mode Imaging. *J. Am. Chem. Soc.* **2013**, *135*, 6494−6503.

(2) Li, K.; Wen, S.; Larson, A. C.; Shen, M.; Zhang, Z.; Chen, Q.; Shi, X.; Zhang, G. Multifunctional Dendrimer-Based Nanoparticles for In

DOI: 10.1021/acsami.5b04359
ACS Appl. Mater. Interfaces 2015, 7, 17287−17297

Vivo MR/CT Dual-Modal Molecular Imaging of Breast Cancer. *Int. J. Nanomed.* **2013**, *8*, 2589−2600.
(3) Liu, C.; Gao, Z.; Zeng, J.; Hou, Y.; Fang, F.; Li, Y.; Qiao, R.; Shen, L.; Lei, H.; Yang, W.; Gao, M. Magnetic/Upconversion Fluorescent NaGdF4: Yb, Er Nanoparticle-Based Dual-Modal Molecular Probes for Imaging Tiny Tumors In Vivo. *ACS Nano* **2013**, *7*, 7227−7240.
(4) Xing, H.; Bu, W.; Zhang, S.; Zheng, X.; Li, M.; Chen, F.; He, Q.; Zhou, L.; Peng, W.; Hua, Y.; Shi, J. Multifunctional Nanoprobes for Upconversion Fluorescence, MR and CT Trimodal Imaging. *Biomaterials* **2012**, *33*, 1079−1089.
(5) Zhu, J.; Lu, Y.; Li, Y.; Jiang, J.; Cheng, L.; Liu, Z.; Guo, L.; Pan, Y.; Gu, H. Synthesis Of Au−Fe_3O_4 Heterostructured Nanoparticles for In Vivo Computed Tomography and Magnetic Resonance Dual Model Imaging. *Nanoscale* **2014**, *6*, 199−202.
(6) Xia, A.; Chen, M.; Gao, Y.; Wu, D.; Feng, W.; Li, F. Gd^{3+} Complex-modified $NaLuF_4$-Based Upconversion Nanophosphors for Trimodality Imaging of NIR-to-NIR Upconversion Luminescence, X-Ray Computed Tomography and Magnetic Resonance. *Biomaterials* **2012**, *33*, 5394−5405.
(7) Chou, S. W.; Shau, Y. H.; Wu, P. C.; Yang, Y. S.; Shieh, D. B.; Chen, C. C. In Vitro and In Vivo Studies of FePt Nanoparticles for Dual Modal CT/MRI Molecular Imaging. *J. Am. Chem. Soc.* **2010**, *132*, 13270−13278.
(8) Ding, J.; Wang, Y.; Ma, M.; Zhang, Y.; Lu, S.; Jiang, Y.; Qi, C.; Luo, S.; Dong, G.; Wen, S.; An, Y.; Gu, N. CT/Fluorescence Dual-Modal Nanoemulsion Platform for Investigating Atherosclerotic Plaques. *Biomaterials* **2013**, *34*, 209−216.
(9) Zhang, J.; Li, C.; Zhang, X.; Huo, S.; Jin, S.; An, F. F.; Wang, X.; Xue, X.; Okeke, C. I.; Duan, G.; Guo, F.; Zhang, X.; Hao, J.; Wang, P. C.; Zhang, J.; Liang, X. J. In Vivo Tumor-Targeted Dual-modal Fluorescence/CT Imaging Using a Nanoprobe Co-Loaded with an Aggregation-Induced Emission Dye and Gold Nanoparticles. *Biomaterials* **2015**, *42*, 103−111.
(10) Lusic, H.; Grinstaff, M. W. X-Ray-Computed Tomography Contrast Agents. *Chem. Rev.* **2013**, *113*, 1641−1666.
(11) Liu, Y.; Ai, K.; Lu, L. Nanoparticulate X-Ray Computed Tomography Contrast Agents: from Design Validation to In Vivo Applications. *Acc. Chem. Res.* **2012**, *45*, 1817−1827.
(12) Lee, N.; Choi, S. H.; Hyeon, T. Nano-Sized CT Contrast Agents. *Adv. Mater.* **2013**, *25*, 2641−2660.
(13) Jakhmola, A.; Anton, N.; Vandamme, T. F. Inorganic Nanoparticles Based Contrast Agents for X-Ray Computed Tomography. *Adv. Healthcare Mater.* **2012**, *1*, 413−431.
(14) Louie, A. Multimodality imaging probes: design and challenges. *Chem. Rev.* **2010**, *110*, 3146−3195.
(15) Liu, T.; Shi, S.; Liang, C.; Shen, S.; Cheng, L.; Wang, C.; Song, X.; Goel, S.; Barnhart, T. E.; Cai, W.; Liu, Z. Iron oxide decorated MoS_2 nanosheets with double PEGylation for chelator-free radiolabeling and multimodal imaging guided photothermal therapy. *ACS Nano* **2015**, *9*, 950−960.
(16) Xia, H. X.; Yang, X. Q.; Song, J. T.; Chen, J.; Zhang, M. Z.; Yan, D. M.; Zhang, L.; Qin, M. Y.; Bai, L. Y.; Zhao, Y. D.; Ma, Z. Y. Folic Acid-Conjugated Silica-Coated Gold Nanorods and Quantum Dots for Dual-Modality CT and Fluorescence Imaging And Photothermal Therapy. *J. Mater. Chem. B* **2014**, *2*, 1945−1953.
(17) Oh, M. H.; Lee, N.; Kim, H.; Park, S. P.; Piao, Y.; Lee, J.; Jun, S. W.; Moon, W. K.; Choi, S. H.; Hyeon, T. Large-Scale Synthesis of Bioinert Tantalum Oxide Nanoparticles for X-Ray Computed Tomography Imaging and Bimodal Image-Guided Sentinel Lymph Node Mapping. *J. Am. Chem. Soc.* **2011**, *133*, 5508−5515.
(18) Xiao, Q.; Bu, W.; Ren, Q.; Zhang, S.; Xing, H.; Chen, F.; Li, M.; Zheng, X.; Hua, Y.; Zhou, L.; Peng, W.; Qu, H.; Wang, Z.; Zhao, K.; Shi, J. Radiopaque Fluorescence-Transparent TaO_X Decorated Upconversion Nanophosphors for In Vivo CT/MR/UCL Trimodal Imaging. *Biomaterials* **2012**, *33*, 7530−7539.
(19) Ai, K.; Liu, Y.; Liu, J.; Yuan, Q.; He, Y.; Lu, L. Large-Scale Synthesis of Bi_2S_3 Nanodots as a Contrast Agent for In Vivo X-Ray Computed Tomography Imaging. *Adv. Mater.* **2011**, *23*, 4886−4891.
(20) Tian, G.; Zheng, X.; Zhang, X.; Yin, W.; Yu, J.; Wang, D.; Zhang, Z.; Yang, X.; Gu, Z.; Zhao, Y. TPGS-Stabilized NaYbF4:Er Upconversion Nanoparticles For Dual-Modal Fluorescent/CT Imaging and Anticancer Drug Delivery to Overcome Multi-Drug Resistance. *Biomaterials* **2015**, *40*, 107−116.
(21) Liu, J.; Bu, W.; Pan, L.; Zhang, S.; Chen, F.; Zhou, L.; Zhao, K.; Peng, W.; Shi, J. Simultaneous Nuclear Imaging and Intranuclear Drug Delivery by Nuclear-Targeted Multifunctional Upconversion Nanoprobes. *Biomaterials* **2012**, *33*, 7282−7290.
(22) Cole, L. E.; Ross, R. D.; Tilley, J. MR.; Vargo-Gogola, T.; Roeder, R. K. Gold Nanoparticles as Contrast Agents in X-Ray Imaging and Computed Tomography. *Nanomedicine* **2015**, *10*, 321−341.
(23) Feng, J.; Chang, D.; Wang, Z.; Shen, B.; Yang, J.; Jiang, Y.; Ju, S.; He, N. A FITC-Doped Silica Coated Gold Nanocomposite for both In Vivo X-Ray CT and Fluorescence Dual Modal Imaging. *RSC Adv.* **2014**, *4*, 51950−51959.
(24) van Schooneveld, M. M.; Cormode, D. P.; Koole, R.; van Wijngaarden, J. T.; Calcagno, C.; Skajaa, T.; Hilhorst, J.; Hart, D. C.; Fayad, Z. A.; Mulder, W. J. M.; Meijerink, A. A Fluorescent, Paramagnetic and PEGylated Gold/Silica Nanoparticle for MRI, CT and Fluorescence Imaging. *Contrast Media Mol. Imaging* **2010**, *5*, 231−236.
(25) Escobedo, J. O.; Rusin, O.; Lim, S.; Strongin, R. M. NIR Dyes for Bioimaging Applications. *Curr. Opin. Chem. Biol.* **2010**, *14*, 64−70.
(26) Luo, S.; Zhang, E.; Su, Y.; Cheng, T.; Shi, C. A Review of NIR Dyes in Cancer Targeting and Imaging. *Biomaterials* **2011**, *32*, 7127−7138.
(27) Lee, C. H.; Cheng, S. H.; Wang, Y. J.; Chen, Y. C.; Chen, N. T.; Souris, J.; Chen, C. T.; Mou, C. Y.; Yang, C. S.; Lo, L. W. Near-Infrared Mesoporous Silica Nanoparticles for Optical Imaging: Characterization and In Vivo Biodistribution. *Adv. Funct. Mater.* **2009**, *19*, 215−222.
(28) Yang, T.; Sun, Y.; Liu, Q.; Feng, W.; Yang, P.; Li, F. Cubic Sub-20 nm $NaLuF_4$-Based Upconversion Nanophosphors for High-Contrast Bioimaging in Different Animal Species. *Biomaterials* **2012**, *33*, 3733−3742.
(29) Xing, H.; Bu, W.; Ren, Q.; Zheng, X.; Li, M.; Zhang, S.; Qu, H.; Wang, Z.; Hua, Y.; Zhao, K.; Zhou, L.; Peng, W.; Shi, J. A $NaYbF_4$:Tm^{3+} Nanoprobe for CT and NIR-to-NIR Fluorescent Bimodal Imaging. *Biomaterials* **2012**, *33*, 5384−5393.
(30) Wu, X.; Chen, G.; Shen, J.; Li, Z.; Zhang, Y.; Han, G. Upconversion Nanoparticles: A Versatile Solution to Multiscale Biological Imaging. *Bioconjugate Chem.* **2015**, *26*, 166−175.
(31) Chen, G.; Qiu, H.; Prasad, P. N.; Chen, X. Upconversion Nanoparticles: Design, Nanochemistry, and Applications in Theranostics. *Chem. Rev.* **2014**, *114*, 5161−5214.
(32) Sun, L. D.; Dong, H.; Zhang, P. Z.; Yan, C. H. Upconversion of Rare Earth Nanomaterials. *Annu. Rev. Phys. Chem.* **2015**, *66*, 619−642.
(33) Sun, Y.; Feng, W.; Yang, P.; Huang, C.; Li, F. The Biosafety of Lanthanide Upconversion Nanomaterials. *Chem. Soc. Rev.* **2015**, *44*, 1509−1525.
(34) Schneider, G.; Decher, G.; Nerambourg, N.; Praho, R.; Werts, M. H. V.; Blanchard-Desce, M. Distance-Dependent Fluorescence Quenching on Gold Nanoparticles Ensheathed with Layer-by-Layer Assembled Polyelectrolytes. *Nano Lett.* **2006**, *6*, 530−536.
(35) Jung, J.; Na, K.; Lee, J.; Kim, K. W.; Hyun, J. Enhanced Surface Plasmon Resonance by Au Nanoparticles Immobilized on a Dielectric SiO_2 Layer On a Gold Surface. *Anal. Chim. Acta* **2009**, *651*, 91−97.
(36) Lee, J. E.; Lee, N.; Kim, T.; Kim, J.; Hyeon, T. Multifunctional Mesoporous Silica Nanocomposite Nanoparticles for Theranostic Applications. *Acc. Chem. Res.* **2011**, *44*, 893−902.
(37) Zhang, R.; Wu, C.; Tong, L.; Tang, B.; Xu, Q. H. Multifunctional Core-Shell Nanoparticles as Highly Efficient Imaging and Photosensitizing Agents. *Langmuir* **2009**, *25*, 10153−10158.
(38) Luo, T.; Huang, P.; Gao, G.; Shen, G.; Fu, S.; Cui, D.; Zhou, C.; Ren, Q. Mesoporous Silica-Coated Gold Nanorods with Embedded Indocyanine Green for Dual Mode X-Ray CT and NIR Fluorescence Imaging. *Opt. Express* **2011**, *19*, 17030−17039.

DOI: 10.1021/acsami.5b04359
ACS Appl. Mater. Interfaces 2015, 7, 17287−17297

(39) Yang, X.; Shi, C.; Tong, R.; Qian, W.; Zhau, H. E.; Wang, R.; Zhu, G.; Cheng, J.; Yang, V. W.; Cheng, T.; Henary, M.; Strekowski, L.; Chung, L. W. K. Near IR Heptamethine Cyanine Dye-Mediated Cancer Imaging. *Clin. Cancer Res.* **2010**, *16*, 2833−2844.
(40) Tan, X.; Luo, S.; Wang, D.; Su, Y.; Cheng, T.; Shi, C. A NIR Heptamethine Dye with Intrinsic Cancer Targeting, Imaging and Photosensitizing Properties. *Biomaterials* **2012**, *33*, 2230−2239.
(41) Chung, T. H.; Wu, S. H.; Yao, M.; Lu, C. W.; Lin, Y. S.; Hung, Y.; Mou, C. Y.; Chen, Y. C.; Huang, D. M. The Effect of Surface Charge on The Uptake and Biological Function of Mesoporous Silica Nanoparticles in 3T3-L1 Cells and Human Mesenchymal Stem Cells. *Biomaterials* **2007**, *28*, 2959−2966.
(42) Yang, X. Q.; Gong, H.; Fu, J. W.; Quan, G. T.; Huang, C.; Luo, Q. M. Molecular Imaging of Small Animals with Fluorescent Proteins: From Projection To Multimodality. *Comput. Med. Imag. Grap.* **2012**, *36*, 259−263.
(43) Yang, X. Q.; Meng, Y. Z.; Luo, Q. M.; Gong, H. High Resolution In Vivo Micro-CT with Flat Panel Detector Based on Amorphous Silicon. *J. X-Ray Sci. Technol.* **2010**, *18*, 381−392.
(44) Reineck, P.; Gómez, D.; Ng, S. H.; Karg, M.; Bell, T.; Mulvaney, P.; Bach, U. Distance and Wavelength Dependent Quenching of Molecular Fluorescence By Au@SiO_2 Core-Shell Nanoparticles. *ACS Nano* **2013**, *7*, 6636−6648.
(45) Proulx, S. T.; Luciani, P.; Derzsi, S.; Rinderknecht, M.; Mumprecht, V.; Leroux, J. C.; Detmar, M. Quantitative Imaging of Lymphatic Function with Liposomal Indocyanine Green. *Cancer Res.* **2010**, *70*, 7053−7062.
(46) Sims, P. J.; Waggoner, A. S.; Wang, C. H.; Hoffman, J. F. Mechanism by which Cyanine Dyes Measure Membrane Potential in Red Blood Cells and Phosphatidylcholine Vesicles. *Biochemistry* **1974**, *13*, 3315−3330.
(47) He, C.; Hu, Y.; Yin, L.; Tang, C.; Yin, C. Effects of Particle Size and Surface Charge on Cellular Uptake and Biodistribution of Polymeric Nanoparticles. *Biomaterials* **2010**, *31*, 3657−3666.
(48) Xiao, K.; Li, Y.; Luo, J.; Lee, J. S.; Xiao, W.; Gonik, A. M.; Agarwal, R. G.; Lam, K. S. The Effect of Surface Charge on In Vivo Biodistribution of PEG-Oligocholic Acid Based Micellar Nanoparticles. *Biomaterials* **2011**, *32*, 3435−3446.
(49) Archana, D.; Singh, B. K.; Dutta, J.; Dutta, P. K. In Vivo Evaluation of Chitosan-PVP-Titanium Dioxide Nanocomposite as Wound Dressing Material. *Carbohydr. Polym.* **2013**, *95*, 530−539.
(50) Zhang, Y.; Liu, J. Y.; Ma, S.; Zhang, Y. J.; Zhao, X.; Zhang, X. D.; Zhang, Z. D. Synthesis of PVP-Coated Ultra-Small Fe_3O_4 Nanoparticles as a MRI Contrast Agent. *J. Mater. Sci.: Mater. Med.* **2010**, *21*, 1205−1210.
(51) Chan, K.; Kostun, L. E.; Tenhaeff, W. E.; Gleason, K. K. Initiated Chemical Vapor Deposition of Polyvinylpyrrolidone-Based Thin Films. *Polymer* **2006**, *47*, 6941−6947.
(52) Shilo, M.; Reuveni, T.; Motiei, M.; Popovtzer, R. Nanoparticles as Computed Tomography Contrast Agents: Current Status and Future Perspectives. *Nanomedicine* **2012**, *7*, 257−269.

DOI: 10.1021/acsami.5b04359
ACS Appl. Mater. Interfaces 2015, 7, 17287−17297